Proceedings of the 9th World Congress on Momentum, Heat and Mass Transfer (MHMT'24)
London, United kingdom – April 11 – 13, 2024
Paper No. ENFHT 261
DOI: 10.11159/enfht24.261

Turbulent Flow Control in a Composite Porous-Fluid System Using Engineered Porous Material

Mohammad Jadidi[1], Yasser Mahmoudi[2]
[1]mohammad.jadidi@manchester.ac.uk; [2]yasser.mahmoudi@manchester.ac.uk
Department of Fluids & Environment, University of Manchester, M13 9PL, United Kingdom

Abstract - This study investigates the impact of engineered porous material with cosumized graded porosity on momentum exchange and heat transfer in composite porous fluid systems using pore-scale large eddy simulation. Two composite porous-fluid systems with identical overall porosity (Φ_Global) of 50% are examined: bottom-up grading (20% to 80%) and top-down grading (80% to 20%). Through flow visualization, we observe fluid leakage from porous to non-porous regions across the porous-fluid interface in both cases. Graded porosity proves effective in regulating this phenomenon, introducing geometric constraints on the flow leakage—the primary mechanism governing momentum exchange and heat transfer across the porous-fluid interface. Distinct characteristics in the development of the turbulent boundary layer on the porous-fluid interface and the turbulent flow structures for the two examined cases highlight the efficacy of engineered porous material with cosumized graded porosity as a passive flow control strategy within porous-fluid systems. In conclusion, our research contributes valuable insights into the application of graded porosity for passive flow control in porous-fluid systems, with potential implications for various engineering applications.

Keywords**:** Porous flow; Turbulent flow; Flow control; Engineered porous material; Graded porosity; Large Eddy Simulation (LES); CFD.

1. Introduction

Turbulent flow control within composite porous-fluid systems [1, 2] represents a dynamic area of research with broad-ranging applications in fields such as fluid dynamics [1, 3] and heat transfer [4, 5]. New insights into flow behaviour and thermal characteristics are being uncovered through pore-scale analysis. While theoretical studies, CFD simulations, and experimental measurements based on pore-level methods have been extensively employed to analyze the flow and thermal field within and over porous media [6-11], there remains a notable gap in the fundamental understanding of the information transfer between porous and non-porous regions and the turbulent boundary development on the porous-fluid interface. This lack of understanding persists even for simplified geometries composed of smoothed and disjointed cubes or spheres, as well as periodic flow configurations that lack stagnation regions and downstream wakes [9, 12, 13].

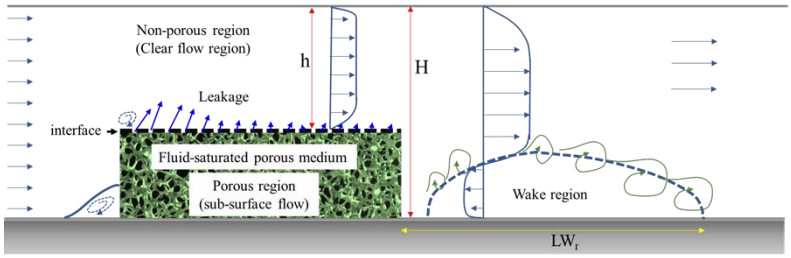

Fig. 1: Schematic of turbulent flow in a composite porous-fluid system: The figure illustrates various flow phenomena, including flow separation at the leading face of the porous block, reattachment of the boundary layer at the porous-fluid interface, wake formation downstream of the porous block, and flow leakage at the interface.

The development of turbulent boundary layer at the porous-fluid interface is a highly complex phenomenon, given that the exchange of momentum between porous and non-porous flows leads to intricate information transfer at the interface [9, 10, 12]. Extensive investigations have been conducted on the momentum exchange and turbulent boundary development near the porous-fluid interface in fully-developed porous channel flows [11, 13-15]. Previous studies [16-18] have shed light on the significance and characteristics of these momentum exchange phenomena in fully-developed porous channel

flows. It has been observed that in these flows, the occurrence of ejection events ($v' < 0$, where v' is the wall-normal velocity fluctuation), which transport fluid from the non-porous to the porous flow across the permeable interface, is statistically correlated with the simultaneous presence of large-scale regions of $u' > 0$, where u' is the streamwise velocity fluctuation in the non-porous flow, and vice versa [9, 13, 19]. This negative correlation between u' and v' leads to the generation of strong ejection and sweep events, as indicated by $u'v' < 0$. Moreover, it is known that permeability enhances the intensity and duration of ejection and sweep events in fully-developed porous channel flows [18].

Recent studies on composite porous-fluid systems, such as those consisting of a porous block immersed in the turbulent channel flow [4, 20, 21], have observed distinct mechanisms for momentum exchange across the porous-fluid interface compared to the fully-developed porous channel flow. It was shown that in these composite systems, information transfer between the porous and non-porous regions is primarily governed by the leakage of the flow from the porous region to the flow passing over it in the non-porous region [1, 22]. Moreover, the formation of turbuetn boundary loyer is compeltly deferenct from the avble finding for fully-developed porous channel flows.

Available findings indicate that the flow through stochastic metal foam is influenced by two primary phenomena: flow leakage and the channelling effect. Flow leakage occurs as fluid enters the porous block from the leading face, particularly in the stagnation region, and exits through preferential pathways at the porous-fluid interface. This leads to non-uniform flow distribution and reduces the residence time of fluid within the porous block. Conversely, the channelling effect refers to the development of high-momentum preferential flow channels within the porous block, resulting in localized jet-like flows. Engineered porous materials with precisely designed local porosity and permeability can serve as effective tools for controlling turbulent flows by manipulating these two significant phenomena governing momentum exchange in a composite porous-fluid system.

Although theoretical studies, CFD simulations, and experimental measurements based on pore-level methods have been extensively employed to analyze the flow and thermal field within and stpchastic porous media and simplified geometries composed of smoothed and disjointed cubes or spheres [6-11], for engineered porous materials there remains a notable gap in the fundamental understanding of the momentum exchange between porous and non-porous regions and the effece of locally vaiaibl porosity and premaability on the control and manipulation of turbulent flows. [9, 12, 13]. This study aims to investigate the mechanisms underlying turbulent flow control within a composite porous-fluid system, utilizing engineered porous materials. The central focus of this study revolves around the concept of Triply Periodic Minimal Surface Structures (TPMS) as the basis for engineered porous materials. These intricate structures offer a unique platform to explore the effects of local porosity variations on the overall flow behavior within the composite system. We aim to provide insights into how different local porosities impact the momentum exchange, which is crucial for turbulent flow control.

2. Methodology

The numerical methodology employed in this investigation incorporates the sophisticated Large Eddy Simulation (LES) approach, acknowledged for its exceptional accuracy in elucidating turbulent flow phenomena within and above porous blocks in composite porous-fluid systems. The selection of the LES technique underscores our commitment to capturing the intricate dynamics of turbulence with a high degree of precision, thereby enhancing the reliability and fidelity of the simulation results.

In a deliberate effort to systematically scrutinize the impact of porosity grading on information transfer between porous and non-porous domains, the study strategically manipulates local porosity in distinct porous block configurations, all maintaining a uniform 50% overall porosity. Specifically, one configuration manifests a gradual decrease in porosity from bottom to top, while another exhibits a converse pattern of increasing porosity, as visually represented in Fig. 2. This methodological approach is meticulously designed to facilitate a comprehensive exploration of the nuanced dynamics governing porosity grading in composite porous-fluid systems.

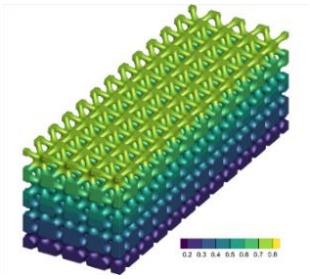

a) GP80_20: Grading Φ_{Local} from 20% to 80%.

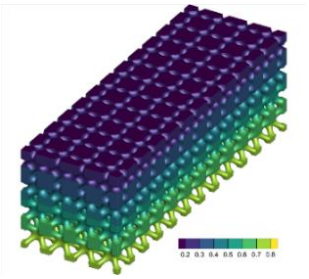

b) GP20_80: Grading Φ_{Local} from 80% to 20%.

Fig. 2: Two different engineered porous materials based on Triply Periodic Minimal Surface Structures (TPMS) with the same overall porosity (Φ_{Global}) of 50%, but different local porosity (Φ_{Local}); **(a)** Bottom-up grading of local porosity from 20% to 80%; **(b)** Top-down grading of local porosity from 80% to 20%.

2.1 Governing Equations

The governing equations for the incompressible flow in the present study are continuity, Navier-Stokes (momentum), and energy equations. Top-hat filtering is applied to the governing equations, resulting in the resolved LES equations as follows [23]:

$$\frac{\partial \overline{u_i}}{\partial x_i} = 0 \tag{1}$$

$$\frac{\partial \overline{u_i}}{\partial t} + \frac{\partial}{\partial x_j}\left(\overline{u_i}\,\overline{u_j}\right) = -\frac{1}{\rho}\frac{\partial \bar{p}}{\partial x_i} + \frac{\partial}{\partial x_j}\left(\upsilon \frac{\partial \overline{u_i}}{\partial x_j} - \tau_{ij}\right) \tag{2}$$

$$\frac{\partial \overline{\Theta}}{\partial t} + \frac{\partial}{\partial x_j}\left(\overline{\Theta}\,\overline{u_j}\right) = \frac{\partial}{\partial x_j}\left((\alpha + \alpha_{SGS})\frac{\partial \overline{\Theta}}{\partial x_j}\right) \tag{3}$$

Here, we use the symbol ($\bar{}$) to denote the filtration operation. Accordingly, the filtered pressure, temperature, and velocity in the i^{th} direction are represented by $\overline{p}$, $\overline{\Theta}$ and $\overline{u_i}$, respectively. To estimate the sub-grid scale (SGS) stress (defined as $\tau_{ij} = \overline{u_i u_j} - \overline{u_i}\,\overline{u_j}$), we employ a localized dynamic k_{SGS}-equation model [24].

The filtered governing equations are discretized by implementing the finite volume method. All the computations are carried out in the open-source object-oriented C++ programming in the OpenFOAM CFD package [14]. The second-order central difference scheme is adopted for spatial discretization. The implicit second-order backward difference scheme is used for the time integration. The PISO is taken on for the pressure–velocity coupling in all the present simulations [15]. To accurately capture the evolution of the flow features, the physical time step is chosen for each grid such that the CFL number is kept below unity. This is true for the most refined portions of each grid enforcing a constant time step of $\Delta t = 1\times10^{-5}\ s$. The time averaging process is begun when the initial transient conditions are washed out and a semi-steady state operating condition is reached. All the present numerical results are averaged over a period of 490 non-dimensional time units ($t^* = t \times U_{in}/h$), where U_{in} is the flow mean velocity at the channel inlet and h is the porous block height. The computational domain is discretized into 169 million non-uniform cells. The grid resolution is assessed based on the two-point correlation that has been implemented by Bazdidi-Tehrani et al. [16]. The Reynolds number based on the inlet channel height and inlet velocity is 20000.

To validate the accuracy of our pore-scale Large Eddy Simulation solver, the velocity and turbulent statistics obtained from our simulations were compared with the experimental measurements of Leu et al. [21]. The comparison was done at two locations, X/D = 1.6 and 3.0, and the results showed good agreement between the first- and second-order statistics of the velocity from the LES calculations and the measured data. Fig. 2 illustrates the comparison of the two datasets. The average and maximum errors for the obtained data at X/D = 1.6 were 16.3% and 27.2%, respectively, while the corresponding errors for the predicted results at X/D = 3.0 were 17.3% and 25.4%.

(a) On interface ($X/D = 1.6$) **(b)** Wake region ($X/D = 3.0$)

Fig. 3: Comparison of first- and second-order velocity statistics obtained from the pore-scale Large Eddy Simulation study with experimental measurements by Leu et al. [21]. The symbol $\langle\,\bar{}\,\rangle$ denotes the time-averaged value of the filtered variable.

1. Results And Discussion

In Fig. 4, the primary observable phenomenon is the upward displacement of a fraction of the fluid entering the porous blocks towards the porous-fluid interface, resulting in its subsequent flow exit from the porous region into the non-porous region, commonly referred to as flow leakage [22]. Analysis of the vertical velocity unveils the occurrence of vertical penetrating flows that obstruct the horizontal channels within the porous block as can be seen in Fig. 5. This obstruction leads to a notable attenuation in the streamwise momentum of the pore flow, particularly evident at elevated porous levels proximal to the interface.

Notably, Fig. 4(a) shows that the narrower flow passage between porous ligaments in the GP20_80 configuration precipitates jetting penetration of high-momentum pore flow into the non-porous region. This penetration induces discernible alterations in the flow structures and turbulence statistics at the interface, topics that will be expounded upon in subsequent subsections. In contrast, for the GP80-20 configuration in Fig. 4(b), where wider gaps between the porous ligaments exist, the exchange of information through flow leakage is comparatively less pronounced than in the PG80_20 case.

(a) Instantaneous vertical velocity for GP20_80 **(b)** Instantaneous vertical velocity for GP80_20

Fig. 4: Contours of instantaneous vertical velocity at the symmetry plane show the flow leakage from the porous region into the non-porous region.

Contours depicting the instantaneous streamwise velocity on the symmetry plane at $z/h = 0$ for the two configurations are presented in Fig. 5, revealing distinct velocity fields between the GP20_80 and GP80_20 cases. The GP20_80 exhibits characteristic flow patterns, including the development of a boundary layer in front of the block, flow separation, and recirculation regions preceding the block, a recirculation and reattachment region on the top permeable wall (porous-fluid interface) of the block, and a downstream flow separation and recirculation region in the wake. Notably, the presence of high porosity at the lower level of the porous block, coupled with wider flow passages for pore flow, results in the formation of channel flows (characterized by high-momentum streamwise pore flows) within the porous region at lower levels proximate to the bottom wall. These channel flows exit the porous block, inducing a jetting effect in the wake, leading to detachment of the wake region from the porous block, as evidenced by the iso-surface of zero streamwise velocity in Fig. 6.

(a) Instantaneous streamwise velocity for GP20_80 **(b)** Instantaneous streamwise velocity for GP80_20

Fig. 5: Contours of instantaneous temperature and streamwise velocity at symmetry plane; **(a, b)** GP20_80; **(c, d)** GP80_20.

Conversely, for the GP80_20 case, the development of a boundary layer on the interface is deficient, and the serration and reattachment of the boundary layer are not observed, as depicted in Fig. 6. Furthermore, the channel flows, in this case, appear weaker due to narrower flow passages and, consequently, higher resistance and pressure drop within the porous block for flow traversing the pore spaces. This discrepancy in channel flow characteristics is reflected in the different wake structures illustrated in Fig. 6. The mean flow, as indicated by streamwise velocity, highlights variations in characteristics between the two cases, encompassing channel flows, wake structures, and boundary layer development on the interface. It is anticipated that the pressure drop experienced by the system under these two configurations will undergo significant changes, a phenomenon currently under investigation in this project.

Instantaneous iso-surfaces of $\bar{u} = 0$ are represented in Fig. 6 to gain a better insight into the formation of primary and secondary recirculation regions and the downstream wake flow. The figures show that for all cases, there exists a recirculation region downstream of the blocks. However, for the GP20_80, the reattachment point moves downstream due to the fluid flow exiting from the pores on the upper level of the porous block, as can be noticed in Fig. 5(b). Inspection of the flow reattachment region behind the porous blocks reveals a large reverse flow zone for GP20_80 compared to the GP80_20 case. The reattachment length in the wake region at the symmetry plane (Z/D=0) is 127% longer for GP20_80 than that in the GP80_20 case. Fig. 6(b) shows that higher porosity on the interface destroys the strong reverse flow pattern of the primary recirculation region into a small local reverse flow pattern.

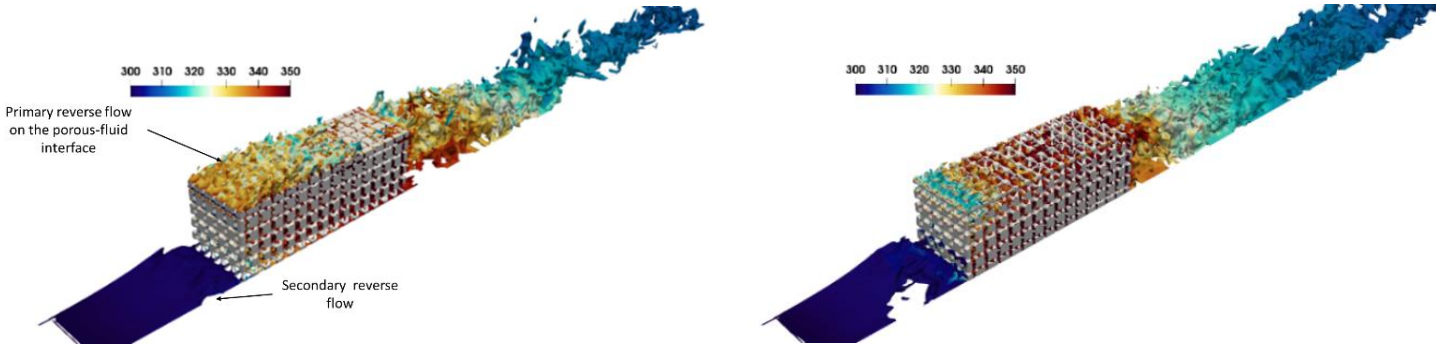

(a) GP80_20 **(b)** GP20_80

Fig. 6: Instantaneous iso-surface of zero streamwise velocity ($\bar{u} = 0$), coloured by instantaneous temperature, illustrating wake structures, boundary layer development on the porous-fluid interface, and the occurrence of reverse flow preceding the porous block.

Fig. 7 presents the instantaneous temperature contours for the two porous block structures, revealing discernible variations in heat transfer mechanisms. The figures distinctly illustrate disparate heat transfer mechanisms employed by the GP20-80 and GP80_20 configurations. In the GP20-80 scenario, the wider flow passages at the lower level of the porous structure facilitate heightened convection through channel flow, promoting effective cooling. Conversely, at the upper level, the constrained flow passages result in a high-temperature flow injection into the non-porous region, driven by the jetting flow or flow leakage. This intricate interplay of convection and injection processes contributes to a nuanced thermal distribution within the GP20-80 configuration.

In contrast, the GP80_20 case manifests a different heat transfer dynamic. The low-temperature flow penetration from the windward face of the porous block at the lower level of the porous block, owing to narrow flow passages, contrasts with the governing influence of momentum exchange at the interface and within the porous and non-porous regions due to wider flow passages. Consequently, the thermal transfer in the GP80_20 configuration is primarily dictated by the ease of momentum exchange on the interface, marking a distinctive departure from the heat transfer mechanisms observed in the GP20-80 configuration.

Anticipated within the scope of ongoing research in this project is a significant disparity in the distribution of heat transfer coefficients between these two porous structures. The intricacies uncovered in this analysis underscore the need for further investigation into the heat transfer dynamics within porous media configurations, with implications for enhancing our understanding of heat exchange processes in such complex systems.

(a) Instantaneous temperature for GP20_80 **(b)** Instantaneous temperature for GP80_20

Fig. 7: Contours of instantaneous temperature at symmetry plane $z/h = 0$ at $Re_h = 20000$.

The flow structures for both cases are visually depicted in Fig. 8, revealing a distinct pattern characterized by a multitude of vortices exhibiting a discernible hairpin structure prominently observed over the interface in all instances. The evolution of these hairpin structures explains a consistent phenomenon across cases, wherein the shear layer, following the leading edge, undergoes circular roll-up, giving rise to a spanwise vortex. Subsequently, this vortex undergoes stretching by the mean shear, ultimately lifting and forming a distinctive hairpin vortex [22]. These observations align with our prior investigations into heat transfer mechanisms mediated by hairpin coherent structures on the interface in porous fluid systems, as documented in [4], and are schematically summarized in Fig. 8(c).

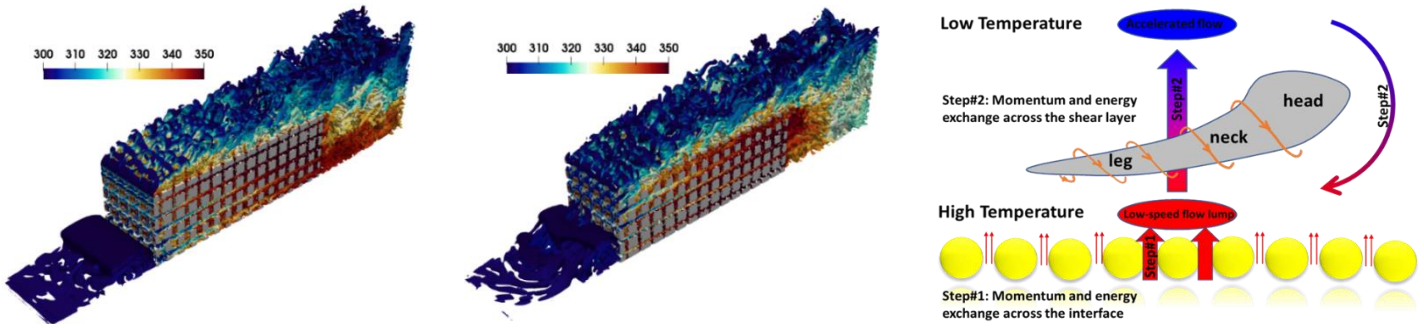

(a) GP20_80 **(b)** GP80_20 **(c)** Schematic representation of momentum and energy exchange mechanisms between porous and non-porous regions [4]

Fig. 8: Evolution of hairpin structures on the interface and the induced mechanisms of heat transfer between porous and non-porous regions

Fig. 9 provides a comprehensive examination of Reynolds stress contours for all cases, revealing distinctive turbulence fluctuation patterns. Notably, for the GP20_80 configuration, two discernible regions of turbulence fluctuation emerge. The first region, characterized by a notably elevated peak value, is situated downstream of the leading edge of the block, coinciding with areas where negative wall-normal velocities manifest (indicative of high-momentum fluid transport toward the interface). At this juncture, flow separation occurs at the leading edge, resulting in the generation of substantial turbulent energy. The turbulence, originating at the upstream edge of the block, rapidly evolves up to approximately $x/h = 2.19$, where

the separated flow re-attaches to the top surface, as depicted in Fig. 6(a). In contrast, the GP80_20 configuration exhibits lower turbulent kinetic energy in this region.

A second region with a secondary peak is identified downstream of the trailing edge, specifically above the leeward face in the GP20_80 case. This region corresponds to the shear layer above the wake region, associated with the upward transport of low-momentum fluid into the outer high-speed flow. In the GP80_20 case, however, the absence of a secondary peak in this region is conspicuous. This observation implies that the reduction in turbulent kinetic energy above the interface is intricately linked to the deterioration of reverse flow, specifically within the primary recirculation region, on the porous-fluid interface, a phenomenon discussed in detail in Fig. 6.

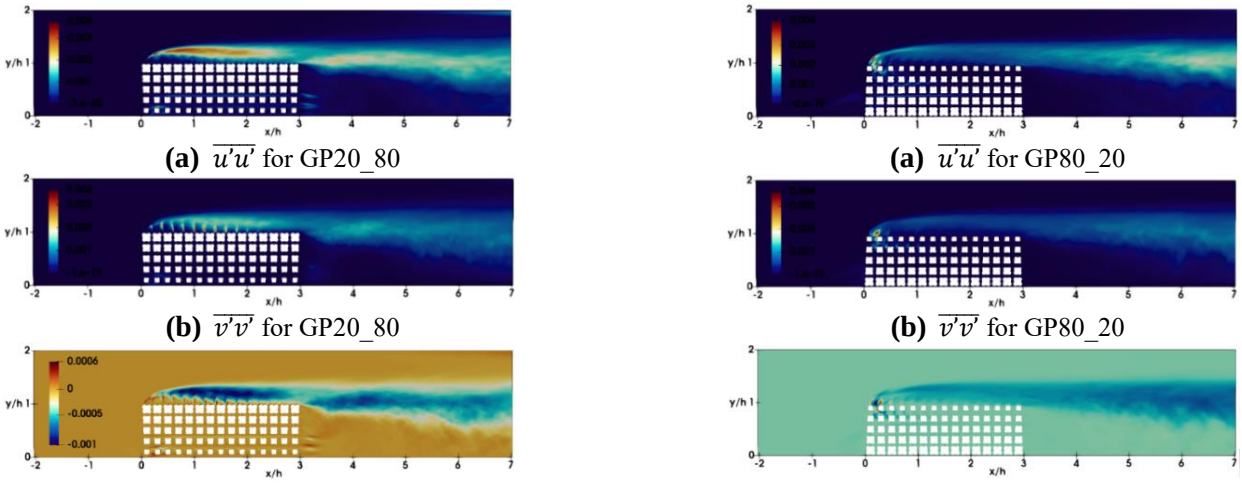

(a) $\overline{u'u'}$ for GP20_80 **(a)** $\overline{u'u'}$ for GP80_20

(b) $\overline{v'v'}$ for GP20_80 **(b)** $\overline{v'v'}$ for GP80_20

(c) $\overline{u'v'}$ for GP20_80 **(c)** $\overline{u'v'}$ for GP80_20

Fig. 9: Contours of Reynolds stress compounds at the symmetry plane z/h = 0 for Re =20000.

Conclusions

In conclusion, flow visualization in our study reveals untapped potential in deliberately manipulating porosity for control and optimization of fluid dynamics in composite porous-fluid systems. As research progresses, insights gained are expected to enhance our understanding of the intricate interplay between graded porosity and turbulent flow. This, coupled with demonstrated porosity manipulation efficacy, is poised to drive the development of advanced strategies for efficient turbulent flow control in diverse engineering applications.

Acknowledgements

This work was supported by the UK Engineering and Physical Sciences Research Council (EPSRC) [grant numbers EP/W033542/1]. Data supporting this publication can be obtained on request. This work used the ARCHER2 UK National Supercomputing Service (https://www.archer2.ac.uk).

References

[1] M. Jadidi, A. Revell, and Y. Mahmoudi, "Pore-scale large eddy simulation of turbulent flow and heat transfer over porous media," *Applied Thermal Engineering*, vol. 215, p. 118916, 2022.

[2] F. S. Anuar, I. A. Abdi, and K. Hooman, "Flow visualization study of partially filled channel with aluminium foam block," *International Journal of Heat and Mass Transfer*, vol. 127, pp. 1197-1211, 2018.

[3] M. Jadidi, H. K. Param, A. Revell, and Y. Mahmoudi, "Flow leakage and Kelvin–Helmholtz instability of turbulent flow over porous media," *Physics of Fluids*, vol. 34, no. 10, 2022.

[4] M. Jadidi, H. K. Param, and Y. Mahmoudi, "On the mechanism of turbulent heat transfer in composite porous-fluid systems with finite length porous blocks: Effect of porosity and Reynolds number," *International Journal of Heat and Mass Transfer*, vol. 208, p. 124006, 2023.
[5] M. Jadidi, H. K. Param, A. Revell, and Y. Mahmoudi, "Large eddy simulations of turbulent heat transfer in packed bed energy storage systems," *Journal of Energy Storage*, vol. 59, p. 106449, 2023/03/01/ 2023, doi: https://doi.org/10.1016/j.est.2022.106449.
[6] K. Vafai, *Handbook of porous media*. Crc Press, 2015.
[7] A. Fathi-kelestani, M. Nazari, and Y. Mahmoudi, "Pulsating flow in a channel filled with a porous medium under local thermal non-equilibrium condition: an exact solution," *Journal of Thermal Analysis and Calorimetry*, vol. 145, no. 5, pp. 2753-2775, 2021/09/01 2021, doi: 10.1007/s10973-020-09843-0.
[8] S. A. Ghorashi, S. A. Hashemi, M. Mollamahdi, M. Ghanbari, and Y. Mahmoudi, "Experimental investigation on flame characteristics in a porous-free flame burner," *Heat and Mass Transfer*, vol. 56, no. 7, pp. 2057-2064, 2020/07/01 2020, doi: 10.1007/s00231-020-02840-x.
[9] T. Kim, G. Blois, J. L. Best, and K. T. Christensen, "Experimental evidence of amplitude modulation in permeable-wall turbulence," *Journal of Fluid Mechanics*, vol. 887, 2020, doi: 10.1017/jfm.2019.1027.
[10] K. Suga, Y. Okazaki, and Y. Kuwata, "Characteristics of turbulent square duct flows over porous media," *Journal of Fluid Mechanics*, vol. 884, 2020, doi: 10.1017/jfm.2019.914.
[11] G. Blois, G. H. Sambrook Smith, J. L. Best, R. J. Hardy, and J. R. Lead, "Quantifying the dynamics of flow within a permeable bed using time-resolved endoscopic particle imaging velocimetry (EPIV)," *Experiments in Fluids*, vol. 53, no. 1, pp. 51-76, 2012, doi: 10.1007/s00348-011-1198-8.
[12] X. Chu, W. Wang, G. Yang, A. Terzis, R. Helmig, and B. Weigand, "Transport of Turbulence Across Permeable Interface in a Turbulent Channel Flow: Interface-Resolved Direct Numerical Simulation," *Transport in Porous Media*, vol. 136, no. 1, pp. 165-189, 2021, doi: 10.1007/s11242-020-01506-w.
[13] W. P. Breugem, B. J. Boersma, and R. E. Uittenbogaard, "The influence of wall permeability on turbulent channel flow," *Journal of Fluid Mechanics*, vol. 562, p. 35, 2006, doi: 10.1017/s0022112006000887.
[14] W. Wang, X. Chu, A. Lozano-Durán, R. Helmig, and B. Weigand, "Information transfer between turbulent boundary layers and porous media," *Journal of Fluid Mechanics*, vol. 920, p. A21, 2021, Art no. A21, doi: 10.1017/jfm.2021.445.
[15] Y. Kuwata and K. Suga, "Extensive investigation of the influence of wall permeability on turbulence," *International journal of heat and fluid flow*, vol. 80, p. 108465, 2019, doi: 10.1016/j.ijheatfluidflow.2019.108465.
[16] G. Rousseau and C. Ancey, "Scanning PIV of turbulent flows over and through rough porous beds using refractive index matching," *Experiments in Fluids*, vol. 61, no. 8, 2020-08-01 2020, doi: 10.1007/s00348-020-02990-y.
[17] Y. Kuwata and K. Suga, "Transport mechanism of interface turbulence over porous and rough walls," *Flow Turbulence and Combustion*, vol. 97, no. 4, pp. 1071-1093, 2016, doi: 10.1007/s10494-016-9759-9.
[18] K. Suga, M. Mori, and M. Kaneda, "Vortex structure of turbulence over permeable walls," *International Journal of Heat and Fluid Flow*, vol. 32, no. 3, pp. 586-595, 2011/06/01/ 2011, doi: https://doi.org/10.1016/j.ijheatfluidflow.2011.02.016.
[19] D. Pokrajac and C. Manes, "Velocity Measurements of a Free-Surface Turbulent Flow Penetrating a Porous Medium Composed of Uniform-Size Spheres," *Transport in Porous Media*, vol. 78, no. 3, p. 367, 2009/02/07 2009, doi: 10.1007/s11242-009-9339-8.
[20] F. Shikh Anuar, I. Ashtiani Abdi, and K. Hooman, "Flow visualization study of partially filled channel with aluminium foam block," *International Journal of Heat and Mass Transfer*, vol. 127, pp. 1197-1211, 2018, doi: 10.1016/j.ijheatmasstransfer.2018.07.047.
[21] J. M. Leu, H. C. Chan, and M. S. Chu, "Comparison of turbulent flow over solid and porous structures mounted on the bottom of a rectangular channel," *Flow Measurement and Instrumentation*, vol. 19, no. 6, pp. 331-337, 2008/12/01/ 2008, doi: 10.1016/j.flowmeasinst.2008.05.001.
[22] M. Jadidi, H. K. Param, A. Revell, and Y. Mahmoudi, "Flow leakage and Kelvin–Helmholtz instability of turbulent flow over porous media," *Physics of Fluids*, vol. 34, no. 10, p. 105114, 2022, doi: 10.1063/5.0111195.
[23] S. B. Pope, *Turbulent Flows*. Cambridge: Cambridge University Press, 2000.
[24] W.-W. Kim, S. Menon, W.-W. Kim, and S. Menon, "Application of the localized dynamic subgrid-scale model to turbulent wall-bounded flows," in *35th aerospace sciences meeting and exhibit*, 1997, p. 210.